DETECTION OF ASEISMIC CREEP ALONG THE SAN ANDREAS FAULT NEAR PARKFIELD, CALIFORNIA WITH ERS-1 RADAR INTERFEROMETRY

Charles L. Werner, Paul Rosen, Scott Hensley, Eric Fielding, and Sean Buckley
Jet Propulsion Laboratory,4800 Oak Grove Drive, Pasadena, California

ABSTRACT

Parkfield, California lies an area along the San Andreas fault in Southern California that has experienced strong earthquakes at apparently regular intervals in historic times. Differential interferometric analysis of ERS data of this region reveals the wide-area distribution of creep along the moving fault segment over a 15 month interval. Removal of the interferometric phase related to the surface topography was done by simulation of an interferogram in the absence of motion given a topographic map of the region. A sharp phase discontinuity in the differential interferogram is equivalent to approximately 1.5 cm change in the line of sight. This displacement is consistent with current models of motion along the fault. We compare the observed phase signature with a predictions of the differential phase based upon the Okada model for elastic deformation. The ERS differential interferometric data are compared with a 6 month differential interferogram collected by the NASA SIR-C L-Band instrument in 1994.

1. INTRODUCTION

Parkfield, California lies an area along the San Andreas Fault (SAF) in Southern California that has experienced moderate earthquakes at apparently regular intervals in historic times [Bakun and Lindh 1985]. It is a site of intense study in anticipation of a significant earthquake ($M_w > 6$) that according to predictions appears long overdue [Roeloffs 1994]. Such an event is

expected because the section of the San Andreas Fault northwest of the town of Parkfield, measured by conventional geodetic methods, is creeping aseismically at a rates consistent with the right lateral secular plate motion, whereas these data also strongly suggest a region beneath Parkfield that is locked and has accumulated a slip deficit greater than the displacement that occurred in the 1966 earthquake [Harris and Segall 1987].

ERS-1 has clearly demonstrated the capability to map earthquakes, [Massonnet et al. 1993] and [Peltzer and Rosen 1995], post seismic rebound, [Peltzer et al. 1995], as well as volcanic deformation, such as at Kilauea in Hawaii [Rosen et al. 1996]. Based on the earlier work on coseismic detection of motion, we proposed to attempt detection of aseismic creep along the San Andreas Fault.

The San Andreas fault is divided into several major sections. The Parkfield segment of the fault is a section of the North American-Pacific plate boundary. Below depths of 10 to 20 km the Pacific and North American plates have a secular motion of 3.5 cm/year. North of Parkfield, aseismic slip and small shocks account for the plate motion, while south of the town, infrequent large earthquakes ($M_w > 7$) release stress buildup. The last time there was motion on this segment of the fault was the 1857 Fort

Tejon earthquake. Parkfield lies in the transition zone and because of constraints on the length of fault rupture in this region, is the site of moderate earthquakes that occur at shorter intervals. Earthquakes of approximately M_w 6 have occurred on 2 February

1881, 3 March 1901, 10 March 1922, 8 June 1934 and 28 June 1966. Based upon statistical analysis of these past events, Parkfield has been the site of a concerted monitoring effort in anticipation of an earthquake that was to have occurred before 1993. Careful measurements of the fault motion have been made using creep meters, two-color geodimeters, and GPS receivers. These in-situ data are an ideal data set for comparison with the creep and deformation measurements derived from ERS-1 repeat track interferometry. The high spatial sampling density of SAR interferometry may give additional insight into the distribution of strain for transition zone.

ERS interferometric analysis must often contend with significant temporal decorrelation. In order to detect fault creep long time intervals between data acquisitions are required such that measureable displacements can occur. While the short ERS wavelength of 5.66 cm has good sensitivity to displacements, small scale surface changes arising from vegetation and precipitation can completely decorrelate a scene [Zebker and Villasenor 1992]. The region around Parkfield is semi-arid and the hope is that correlation over long time intervals should be present.

2. ERS-1 AND SIR-C DATA PROCESSING

Criteria for selection of the ERS data scenes for Parkfield was a combination of interval between acquisitions and the baseline length. The catalog of interferometric baselines supplied by ESA were searched to find combinations acquisitions with time durations exceeding 6 months and with baselines less than 200 meters. Data were ordered from frames 2871 and 2889 and orbits including 4180, 5182, 10192, and 11194. The most promising interferometric pair was 4180 and 10192 covering a time interval of 420 days and a perpendicular baseline B_{perp} of only 3 meters. Starting with the raw ERS data, SLC images were produced to

maximize the interferometric correlation by choosing a common doppler centroid. An interferogram was produced using standard processing algorithms [Zebker et al. 1994].

The interferometric phase is a combination of topographic and displacement related components. If the phase trend associated with the curved earth is removed, then the interferometric phase is given by:

$$\phi_{flat} = -\frac{4\pi}{\lambda} B_{perp} \frac{z}{r_0 \sin\theta_0} + \frac{4\pi}{\lambda}\delta_r \qquad (1)$$

where λ is the wavelength, r_0 and θ_0 the slant range and look angle at the center of the scene respectively, and δ_r the motion of

the surface along the line of sight between data acquisitions [Rosen et al. 1996]. For this interferometric pair the sensitivity to displacement is 1.0×10^5 the sensitivity to topography. None the less, the topographic contribution to the phase must be

subtracted to detect any fault creep.

The interferometric simulator described in [Rosen et al. 1996] was used to generate a synthetic interferogram of the ERS frame using USGS 30 and 90 meter DEMs as input. The simulated interferogram has continuous phase, and does not require phase unwrapping. After precise corregistration and resampling the simulated interferogram relative to the ERS interferogram it can be can be subtracted leaving the residual phase containing the deformation or creep signature. Tropospheric water vapor contributes significant noise on the order of 2π radians to the 2-pass differential interferogram [Goldstein 1995]. The only effective means, at present, for removal of the tropospheric water vapor phase distortion is by averaging of multiple interferograms. The differential interferogram from our single pair is shown in Fig.1.

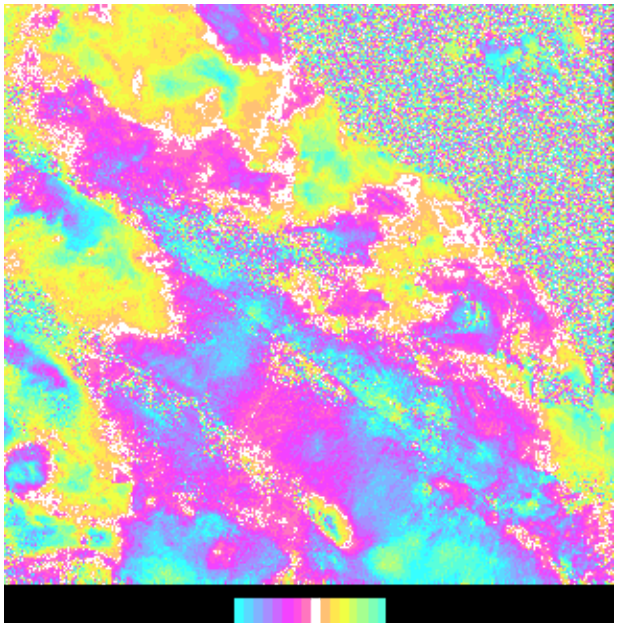

Figure 1: ERS-1 differential interferogram of San Andreas Fault slip near Parkfield California. One color cycle corresponds to a fault motion of 2.84 cm. along the line of sight. Image covers ERS-frame 2871 from orbits 4180 and 10192.

Temporal decorrelation of th data places this data set at the limits of what can be processed. The interferometric correlation coefficient was extremely low (< 0.2) over much of the scene such that only by a extensive averaging could the creep signature be made visible. A new variable resolution filtering algorithm [Goldstein and Werner 1997] was applied that makes use of the fact that the fringe spectrum is generally narrow band relative to the uncorrelated noise spectrum. In this algorithm, the normalized interferogram is divided into 32x32 patches. Each of the patches $S(x,y)$ is Fourier transformed to give $S(u,v)$ and then weighted by the scaled magnitude of the spectrum:

$$\tilde{S}(u,v) = |S(u,v)|^{\alpha} S(u,v) \; . \qquad (2)$$

The filtered signal is obtained by inverse Fourier transform of the filtered patch $\tilde{S}(u,v)$. The output image is formed by summing

overlapping filtered patches using triangular window weighting in both range and azimuth. The interferogram filtered using the new algorithm had significantly better resolution and fringe visibility compared with the interferogram filtered using a fixed resolution smoothing kernel.

Similar processing was performed for tracks of the SIR-C radar that crossed the Parkfield fault zone with a 6 month interval (April and October) between passes in 1994 [Rosen et al. 1996]. Data were acquired at both C- and L-Band, but only the L-Band data had sufficient coherence to be of any value. These data were processed similarly as the ERS data and mosaiked into the ERS scene. One of the advantages of the 2-pass simulation approach to differential interferometry is that geocoding of the data once the simulation has been performed is a simple because the correspondence between the image and topographic map can be stored as a mapping file. Once the data are geocoded, different passes and tracks can be merged. In this case the ERS and SIR-C were mosaiked and then compared.

3. SAN ANDREAS FAULT SLIP MODEL

The Parkfield deformation modeling was performed using a finite-source dislocation buried in an elastic half-space [Feigl and Dupre 1996] based upon the original work by Okada [Okada 1985]. Specifically, the model was used to determine the component of the displacement field in the direction of the radar line-of-sight direction. One cycle of the color wheel corresponds to 28.4 mm of surface deformation in the radar line-of-sight direction.

The creep meters used in the modeling were located at Slack Canyon (xsc1), Middle Mountain (xmm1), Parkfield (xpk1), Work Ranch (wkr1), Carr Ranch (crr1) and Gold Hill (xgh1). The creep meters were assumed to be co-located with the SAF such that their positions could be used to defined fault segments. Specifically, the fault segments were defined by the creep meter locations as follows:

segment i Easting = creep meter i Easting (x)
segment i Northing = creep meter i Northing (y)
segment i $\mathrm{length} = sqrt(x^2 + y^2)$

segment i $\mathrm{strike} = \mathrm{atan2}(x,y) + 2\pi$

segment i $\mathrm{dip} = 90$ degrees

For the northern most fault segment (which corresponded to one creep meter location), the length was set to a sufficiently large number and the strike was set to the adjacent fault segment strike.

The slip along each fault segment was modeled as two separate slip mechanisms: shallow slip and at-depth slip. The shallow slip was modeled with faults segments as defined above with depths of 14 km, widths of 25 km [Harris and Segall 1987] and right lateral fault slip rates as determined from USGS creep meter data spanning the decade 1987.22 to 1997.14 with the secular trend removed [Langbein 1997]:

Slack Canyon (xsc1)	21.15 mm/yr
Middle Mountain (xmm1)	16.68 mm/yr
Parkfield (xpk1)	10.02 mm/yr
Work Ranch (wkr1)	8.49 mm/yr
Carr Ranch (crr1)	3.66 mm/yr
Gold Hill (xgh1)	3.45 mm/yr

The at-depth slip was modeled with a locking depth of 14 km and a right lateral fault slip rate of 25 mm/yr [Harris and Segall 1987] for all fault segments. The expected signature for the differential interferometric pair is shown in Fig. 2

Figure 2: Simulation of ERS differential interferogram based based upon deformations predicted by the Okada model as implemented by Feigl and Dupre. Image covers ERS-frame 2871 from orbits 4180 and 10192. One fringe cycle is equivalent to a displacement along the LOS of 28.4 mm

4. CONCLUSIONS

The fault is clearly visible in the differential interferogram. The magnitude of the tropospheric water vapor phase distortions is greater than the signal an hinders quantitative analysis beyond order of magnitude calculations. A linear phase discontinuity, coincident with the 100 km long fault trace, is equivalent to approximately 1.5 cm change in the line of sight distance. This displacement is consistent with the model of fault motion that we have derived from the creep meter data as input to the Okada elastic deformation model.

The SIR-C data suffer also from tropospheric phase noise, and a shorter time interval. None the less, the higher correlation over the time interval suggests that L-Band decorrelates less rapidly than C-Band. The observed phase signature is consistent with the ERS-1 results.

Quantitative analysis of aseismic creep requires multiple data acquisitions to suppress atmospheric noise. Further study of this region will require systematic processing of all candidate interferometric pairs.

This work was carried out by the Jet Propulsion Laboratory, California Institute of Technology, under a contract with the National Aeronautics and Space Administration

---

References

Bakun and Lindh 1985
Bakun, W. H. and A. G. Lindh, The Parkfield, California earthquake prediction experiment, *Science, 229,* 1985.

Feigl and Dupre 1996
Feigl, K. L. and E. Dupre, RNGCHN: A Program to calculate displacement components from dislocations in an elastic half-space with applications for modeling geodetic measurements of crustal deformation, *Computers and Geosciences,* July 10, 1996.

Goldstein 1995
Goldstein, R. M., Atmospheric limitations to repeat-track radar interferometry, *Geophysical Research Letters 22,* 2517-2520, 1995.

Goldstein et al. 1988
Goldstein, R. M., H. A. Zebker, and C. L. Werner, Satellite radar interferometry: two-dimensional phase unwrapping, *Radio Science, 23,*, 713-720, 1988.

Goldstein and Werner 1997
Goldstein, R. M., and C. L. Werner, Radar ice motion interferometry, to appear in *Proceedings of the* 3^{rd} *ERS Symposium,* Florence, Italy, 18-22 March, 1997.

Harris and Segall 1987

Harris, Ruth A, and P. Segall, Detection of a locked zone at depth on the Parkfield, California, segment of the San Andreas Fault, *Journal of Geophysical Research, 92,* 7945-7962, 1987.

Langbein 1997
Langbein, J., Parkfield creep meter data: detrended measurements from the past 10 years, *http: //quake.wr.usgs.gov /QUAKES/geodetic /twocolor/ creep_pkf_10yr_det.gif*.

Massonnet et al. 1993
Massonnet, D., M. Rossi, C. Carmona, F. Adragna, G.Peltzer, K. Fiegl, and T. Rabaute, The displacement field of the Landers earthquake mapped by radar interferometry, *Nature, 364,* 138-142, 1993.

Okada 1985
Okada, Yoshimitsu, Surface deformation due to shear and tensile faults in a half-space, *Bulletin of the Seismological Society of America, 75,* 1135-1154, 1985.

Peltzer et al. 1995
Peltzer, G., P. A. Rosen, Francois Rogez, and Ken Hudnut, Postseismic rebound in fault step-overs caused by pore fluid flow,, *Science, 273*, 1202-1204, 1996.

Peltzer and Rosen 1995
Peltzer, G. and P. A. Rosen, Surface displacement of the 17 May 1993 Eureka Valley, California, earthquake observed by SAR interferometry, *Science, 268*, 133-1336, 1995.

Roeloffs 1994
Roeloffs, E., The earthquake prediction experiment at Parkfield, California. *Reviews of Geophysics, 32,* 315-335, 1994.

Rosen et al. 1996
Rosen, P. A., S. Hensley, H. A. Zebker, F. H. Webb, and E. J. Fielding, Surface deformation and coherence measurements of Kilauea Volcano, Hawaii, from SIR-C radar interferometry, *Journal of Geophysical Research 101,* 23109-23125, 1996.

Zebker et al. 1994
Zebker, H.A., C. L. Werner, P. A. Rosen, and S. Hensley, Accuracy of topographic maps derived from ERS-1 interferometric radar, *IEEE Trans. Geosci. Remote Sens., 32,* 823-836, 1994.

Zebker and Villasenor 1992
Zebker, H. A., and J. Villasenor, Decorrelation in interferometric radar echoes, *IEEE Trans Geoscience and Remote Sensing, 30,* 950-959, 1992.

Charles L. Werner
Tue Dec 30 11:31:34 PST 1997